SFN Letters速報ゼミ

April 23, 2021

古屋 玲

#338 21-26担当

21. **Revealing a Centrally Condensed Structure in OMC-3/MMS 3 with ALMA High Resolution Observations**

Kaho Morii, Satoko Takahashi, Masahiro N. Machida ★ Using the Atacama Large Millimeter/submillimeter Array (ALMA), we investigated a peculiar millimeter source MMS 3 located in the Orion Molecular Cloud 3 (OMC-3) region in the 1.3 mm continuum, CO (J=2-1), SiO (J=5-4), $C^{18}O$ (J=2-1), N_2D^+ (J=3-2), and DCN (J=3-2) emissions. With the ALMA high angular resolution (∼0".2), we detected a very compact and highly centrally condensed continuum emission with a size of 0".45 × 0".32 (P.A.=0.22°). The peak position coincides with the locations of previously reported *Spitzer*/IRAC and X-ray

22. **Principal component analysis tomography in near-infrared integral field spectroscopy of young stellar objects. I. Revisiting the high-mass protostar W33A**

Felipe Navarete, Augusto Damineli, João E. Steiner, Robert D. Blum ★ W33A is a well-known example of a high-mass young stellar object showing evidence of a circumstellar disc. We revisited the K-band NIFS/Gemini North observations of the W33A protostar using principal components analysis tomography and additional post-processing routines. Our results indicate the presence of a compact rotating disc based on the kinematics of the CO absorption features. The position-velocity

14 を参照

23. **Resolving Structure in the Debris Disk around HD 206893 with ALMA**

Ava Nederlander, A. Meredith Hughes, Anna J. Fehr, Kevin M. Flaherty, Kate Y. L. Su, Attila Moor, Eugene Chiang, Sean M. Andrews, David J. Wilner, Sebastian Marino ★ Debris disks are tenuous, dusty belts surrounding main sequence stars generated by collisions between planetesimals. HD 206893 is one of only two stars known to host a directly imaged brown dwarf orbiting interior to its debris ring, in this case at a projected separation of 10.4 au. Here we resolve structure in the debris disk around HD 206893 at an angular resolution of 0.6" (24 au) and wavelength of 1.3 mm with the Atacama Large Millimeter/submillimeter Array (ALMA). We observe a broad disk extending from a radius of < 51 au to 194^{+13}_{-2}

01 から 06 を参照

24. **Deciphering the 3-D Orion Nebula-III: Structure on the NE boundary of the Orion-S Embedded Molecular Cloud**

C. R. O'Dell, G. J. Ferland, N. P. Abel ★ We have extended the work of Papers I and II of this series to determine at higher spatial resolution the properties of the embedded Orion-S Molecular Cloud that lies within the ionized cavity of the Orion Nebula and of the thin ionized layer that lies between the Cloud and the observer. This was done using existing and new

25. **Deciphering the 3-D Orion Nebula-IV: The HH 269 flow emerges from the Orion-S Embedded Molecular Cloud**

C. R. O'Dell, N. P. Abel, G. J. Ferland ★ We have extended the membership and determined the 3-D structure of the large (0.19 pc) HH 269 sequence of shocks in the Orion Nebula. All of the components lie along a track that is highly tilted to the plane-of-the-sky and emerge from within the Orion-S embedded molecular cloud. Their source is probably either the highly

HSTデータ解析のシリーズ論文

26. **Fiery Cores: Bursty and Smooth Star Formation Distributions across Galaxy Centers in Cosmological Zoom-in Simulations**

Matthew E. Orr, H Perry Hatchfield, Cara Battersby, Christopher C. Hayward, Philip F. Hopkins, Andrew Wetzel, Samantha M. Benincasa, Sarah R. Loebman, Mattia C. Sormani, Ralf S. Klessen ★ We present an analysis of the $R \lesssim 1.5$ kpc core regions of seven simulated Milky Way mass galaxies, from the FIRE-2 (Feedback in Realistic

07 から 13 を参照

23. **Resolving Structure in the Debris Disk around HD 206893 with ALMA**
Ava Nederlander, A. Meredith Hughes, Anna J. Fehr, Kevin M. Flaherty, Kate Y. L. Su, Attila Moor, Eugene Chiang, Sean M. Andrews, David J. Wilner, Sebastian Marino ★ Debris disks are tenuous, dusty belts surrounding

Debris disks are tenuous, dusty belts surrounding main sequence stars generated by collisions between planetesimals. HD 206893 is one of only two stars known to host a directly imaged brown dwarf orbiting interior to its debris ring, in this case at a projected separation of 10.4 au. Here we resolve structure in the debris disk around HD 206893 at an angular resolution of 0.″6 (24 au) and wavelength of 1.3 mm with the Atacama Large Millimeter/submillimeter Array (ALMA). We observe a broad disk extending from a radius of < 51 au to 194^{+13}_{-2} au. We model the disk with a continuous, gapped, and double power-law model of the surface density profile, and find strong evidence for a local minimum in the surface density distribution near a radius of 70 au, consistent with a gap in the disk with an inner radius of 63^{+8}_{-16} au and width 31^{+11}_{-7} au. Gapped structure has been observed in four other debris disks – essentially every other radially resolved debris disk observed with sufficient angular resolution and sensitivity with ALMA – and could be suggestive of the presence of an additional planetary-mass companion.

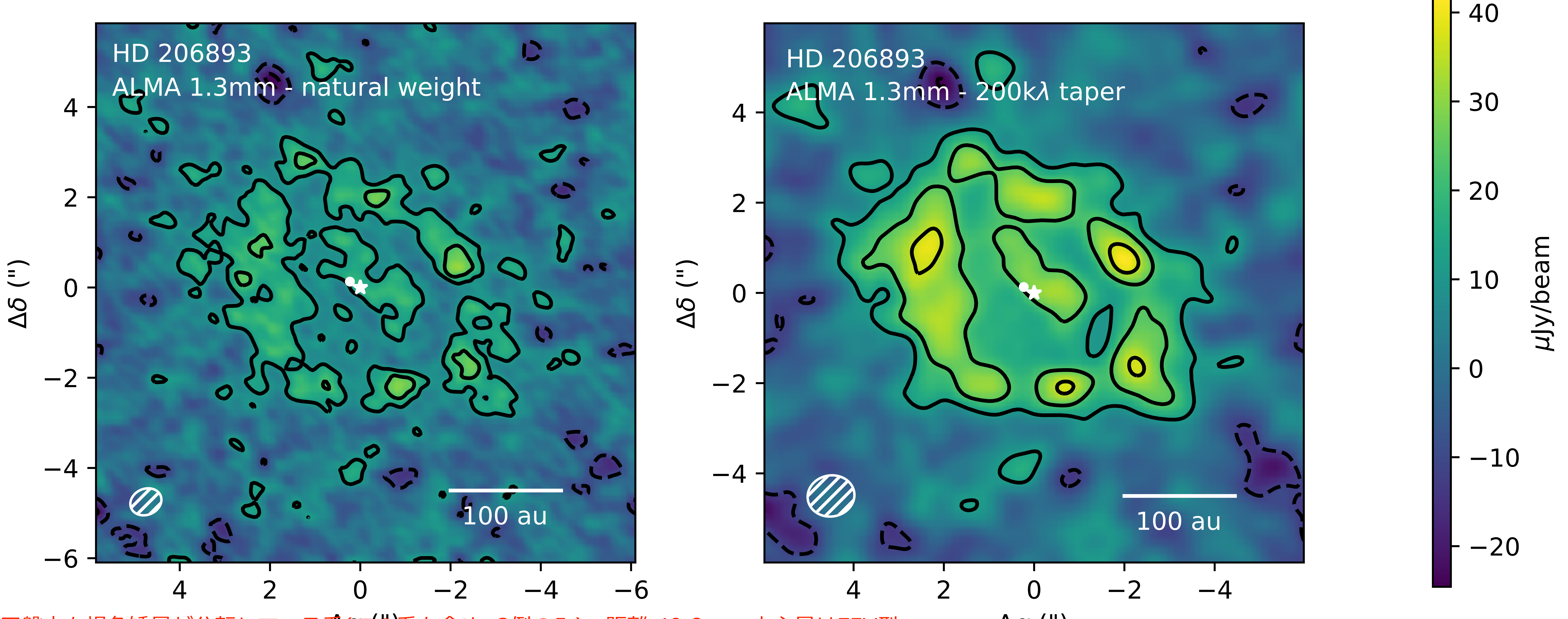

残骸円盤内を褐色矮星が公転している系(この系を含め, 2例のみ) ; 距離 40.8 pc; 中心星はF5V型

Hershell 70 μm画像 plus SED解析 ⇨ $R_{\rm inner} \simeq 50$ AUは推定されていた; 褐色矮星伴星がL5-L9型, ~12 $M_{\rm jup}$, age ~ 50 Myrsも推定されていた.

分光観測(Grandjean+2019)から第3の天体(惑星？BD?)の存在も示唆されていた.

Figure 1. (Left) Naturally weighted ALMA image of the 1.3 mm continuum emission from the HD 206893 system. (Right) Same image with a visibility-domain taper of 200 kλ applied to bring out the large-scale structure of the source. In both panels, contour levels are [-2,2,4,6]×σ, where σ is the rms noise in the image: 5.5 μJy beam^{-1} for the naturally weighted image and 6.0 μJy beam^{-1} for the image with the taper. The hatched ellipse in the lower left corner represents the size and orientation of the synthesized beam: 0.″71×0.″58 for the naturally weighted image and 0.″9×1.″0 for the tapered image. The star symbol represents the pointing center of the observations, i.e., the expected position of the star including a proper motion correction, and the dot represents the position of the brown dwarf companion directly imaged by Milli et al. (2017).

中心星と伴星の褐色矮星の諸元：先行研究から

A&A 608, A79 (2017)
DOI: 10.1051/0004-6361/201731145

Astronomy & Astrophysics

In-depth study of moderately young but extremely red, very dusty substellar companion HD 206893B★

P. Delorme[1,★★], T. Schmidt[2], M. Bonnefoy[1], S. Desidera[3], C. Ginski[4,26], B. Charnay[2], C. Lazzoni[3], V. Christiaens[5,23],

これが主題の
褐色矮星

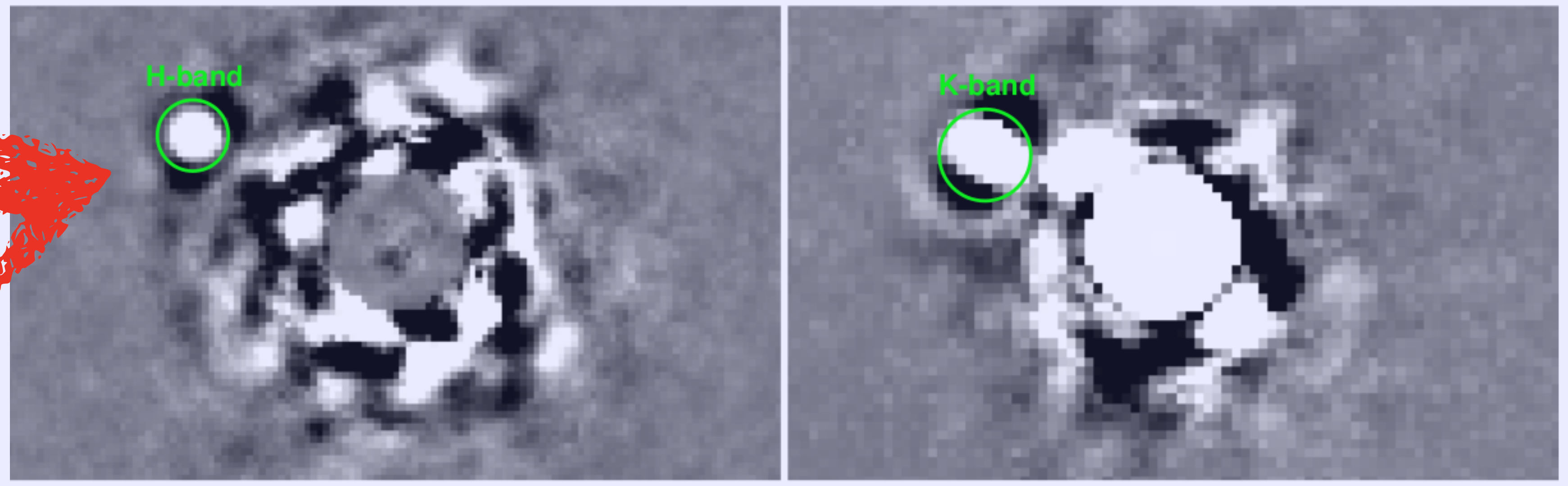

Fig. 3. Residual images of HD 206893B in Y, J, H, and K bands in linear scale. The scale is identical in Y, J, and H, but is 4 times wider in K to accommodate the brighter speckle residuals and brighter companion in the IRDIS K-band image.

Table 1. Stellar parameters of HD 206893. 中心星の諸元

Parameter	Value	Ref.
V (mag)	6.69	Hipparcos
$B-V$ (mag)	0.439	Hipparcos
$V-I$ (mag)	0.51	Hipparcos
J (mag)	5.869 ± 0.023	2MASS
H (mag)	5.687 ± 0.034	2MASS
K (mag)	5.593 ± 0.021	2MASS
Parallax (mas)	24.59 ± 0.26	*Gaia* DR1
μ_α (mas yr^{-1})	94.236 ± 0.044	*Gaia* DR1
μ_δ (mas yr^{-1})	0.164 ± 0.031	*Gaia* DR1
RV (km s^{-1})	−11.92 ± 0.32	this paper
U (km s^{-1})	−20.15 ± 0.23	this paper
V (km s^{-1})	−7.40 ± 0.15,	this paper
W (km s^{-1})	−3.40 ± 0.26	this paper
$T_{\rm eff}$ (K)	6500 ± 100	this paper
log g	4.45 ± 0.15	this paper
[Fe/H]	+0.04 ± 0.02	this paper
EW Li (mÅ)	28.5 ± 7.0	this paper
A(Li)	2.38 ± 0.10	this paper
[Ba/Fe]	0.20 ± 0.20	this paper
$v \sin i$ (km s^{-1})	32 ± 2	this paper
log $L_X/L_{\rm bol}$	−4.80 ±	this paper
log $R_{\rm HK}$	−4.77 ±	this paper
$P_{\rm rot}$ (d)	0.996 ± 0.003	this paper
Age (Myr)	250^{+450}_{-200}	this paper
$M_{\rm star}$ ($M_\odot$)	1.32 ± 0.02	this paper
$R_{\rm star}$ ($R_\odot$)	1.26 ± 0.02	this paper
i (deg)	30 ± 5	this paper

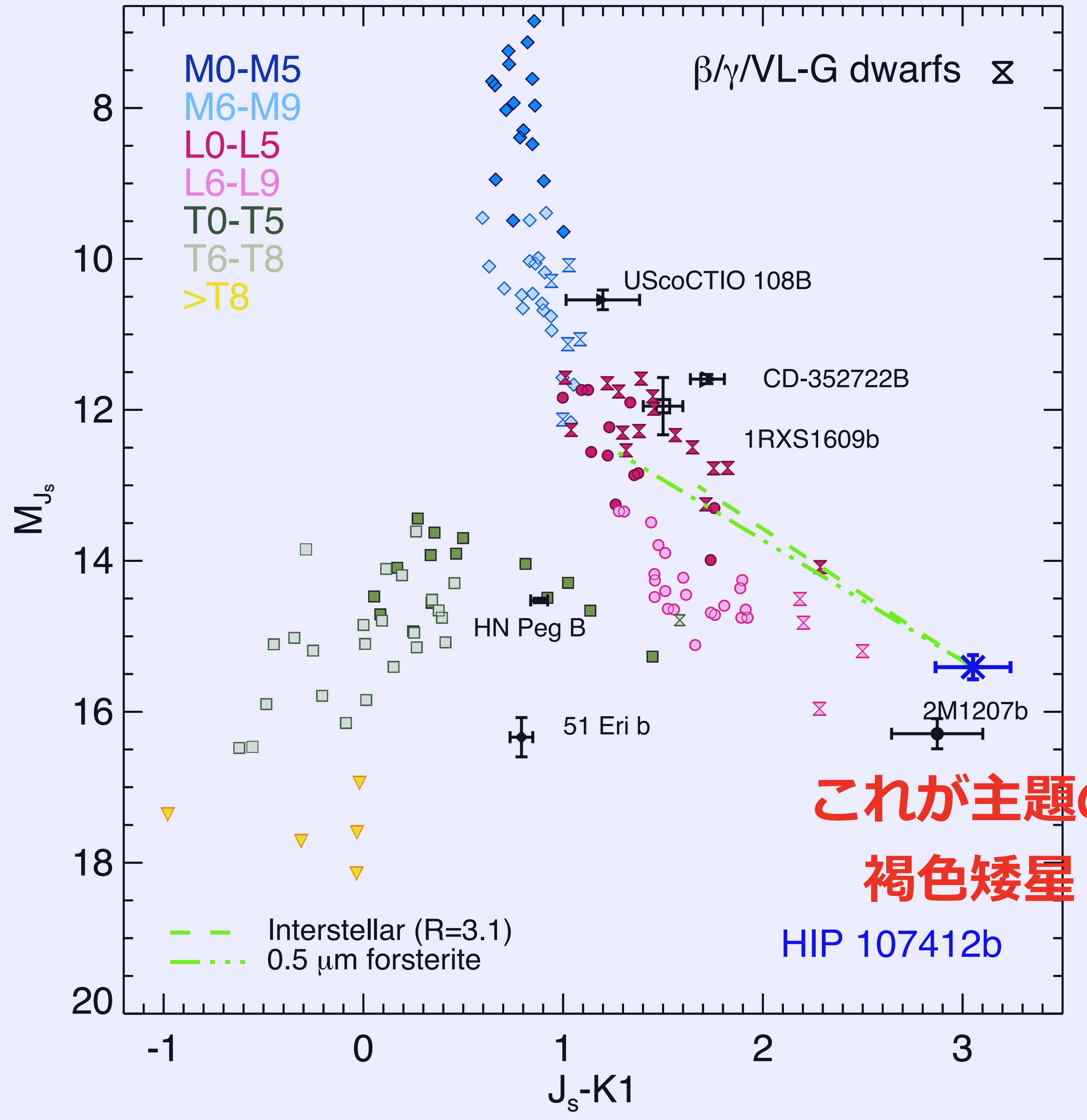

Fig. 7. Placement of the IRDIS photometry of HD 206893B (HIP 1074 to the reddening vector caused by forsterite grains with mean size 0.5 μ parameter R = 3.1).

Methods. We conducted a follow-up of the companion with adaptive optics imaging and spectro-imaging with SPHERE, and a multi-instrument follow-up of its host star. We obtain a R = 30 spectrum from 0.95 to 1.64 μm of the companion and additional photometry at 2.11 and 2.25 μm. We carried out extensive atmosphere model fitting for the companions and the host star in order to derive their age, mass, and metallicity.

Results. We found no additional companion in the system in spite of exquisite observing conditions resulting in sensitivity to 6 $M_{\rm Jup}$ (2 $M_{\rm Jup}$) at 0.5″ for an age of 300 Myr (50 Myr). We detect orbital motion over more than one year and characterise the possible Keplerian orbits. We constrain the age of the system to a minimum of 50 Myr and a maximum of 700 Myr, and determine that the host-star metallicity is nearly solar. The comparison of the companion spectrum and photometry to model atmospheres indicates that the companion is an extremely dusty late L dwarf, with an intermediate gravity (log g ~ 4.5–5.0) which is compatible with the independent age estimate of the system.

Conclusions. Though our best fit corresponds to a brown dwarf of 15–30 $M_{\rm Jup}$ aged 100–300 Myr, our analysis is also compatible with a range of masses and ages going from a 50 Myr 12 $M_{\rm Jup}$ planetary-mass object to a 50 $M_{\rm Jup}$ Hyades-age brown dwarf. Even though this companion is extremely red, we note that it is more probable that it has an intermediate gravity rather than the very low gravity that is often associated with very red L dwarfs. We also find that the detected companion cannot shape the observed outer debris disc, hinting that one or several additional planetary mass objects in the system might be necessary to explain the position of the disc inner edge.

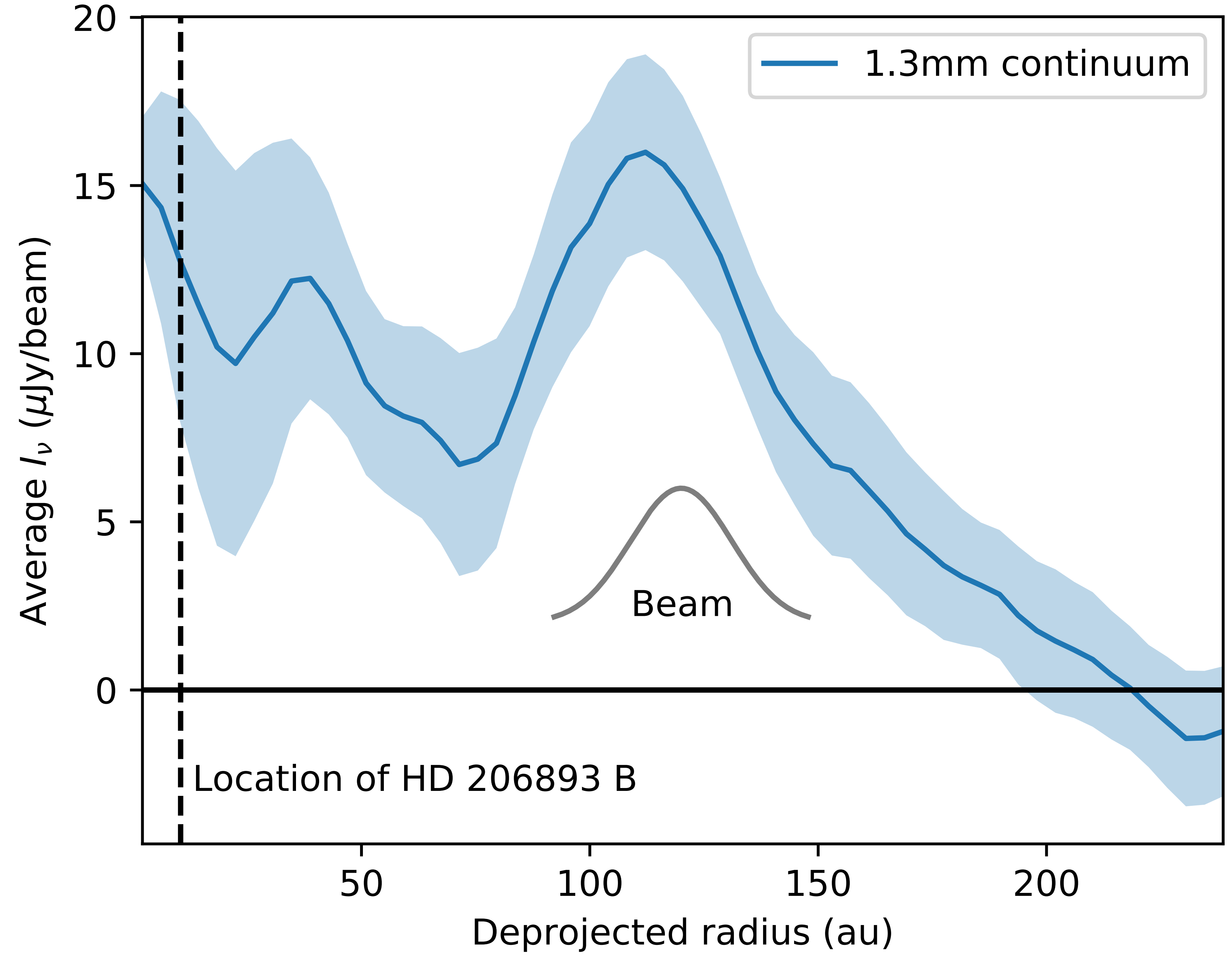

Figure 2. Azimuthally averaged radial intensity profile of the naturally weighted image, deprojected along elliptical contours assuming a circular geometry and an inclination to the line of sight of 45° and position angle of 60°. The blue shaded region represents the standard error of the mean for each radial bin, where the standard deviation is calculated for all pixels within the bin and then divided by the square root of the number of beams sampled. The size of the synthesized beam is indicated by the gray Gaussian marked "Beam." The 10.4 au projected separation of HD 206893 B (Milli et al. 2017) is marked with a vertical dashed line.

$$T_{\rm dust} = \left(\frac{L_*}{16\pi\sigma R^2}\right)^{1/4}$$

nosity of the star, σ is the Stefan-Boltzmann c

We adopt a stellar luminosity of $L_* = 2.83\,{\rm L}_\odot$

これは中心星の光度

$$\Sigma(R) = \Sigma_c R^p \quad (2)$$

between radii of $R_{\rm in}$ and $R_{\rm out}$, where Σ_c is a normalization for the total dust mass in the disk, $M_{\rm disk}$ (see Table 4 for definition), and p is a power law index that we initially set to a value of 1.0. While the value of p is interesting from the perspective of debris disk evolution, there is a well-known degeneracy between p and the location of the outer radius $R_{\rm out}$ (see, e.g., section 4.2.2. of Ricarte et al. 2013) and our data are of sufficiently limited sensitivity and angular resolution that we chose to focus on $R_{\rm out}$ rather than p. We chose a value of 1 as a middle-of-the-road

$R_{\rm out}$とpは縮退していることが知られていること, $R_{\rm out}$を知りたいので，p=1を仮定

Ricci et al. (2015). However, we found that the double power law transition radius fell on the peak in the surface brightness around 115 au, which meant that we were not able to evaluate whether a break in the power-law surface density could reproduce the observed surface brightness profile as well as a disk with a gap. We therefore explored two additional profiles: a double power-law with a radial gap, and a triple power-law with two transitional radii. All of the models were consistent in preferring a dip in the radial surface density profile near 75 au and a peak near 115 au, and the comparison between the latter two functional forms demonstrates that an empty gap with sharp edges yields comparable results to a more shallow power-law inflection point and is preferred with modest statistical significance. Table 4 presents a summary of the functional forms, surface density normalization, free parameters, and best-fit lnprob values for each of the seven classes of models that we fit to the data. For the remainder of the paper, we focus on the comparison between the flat disk (which ignores the local maximum and minimum of the surface density), the double power law with a gap, and the triple power law, since the latter two were the models that best (statistically and by eye) reproduced the features of the observations. 結局、目も含めて判断

The limits of the priors for all parameters are listed in Table 2. For the flat disk we used 16 walkers and ran the

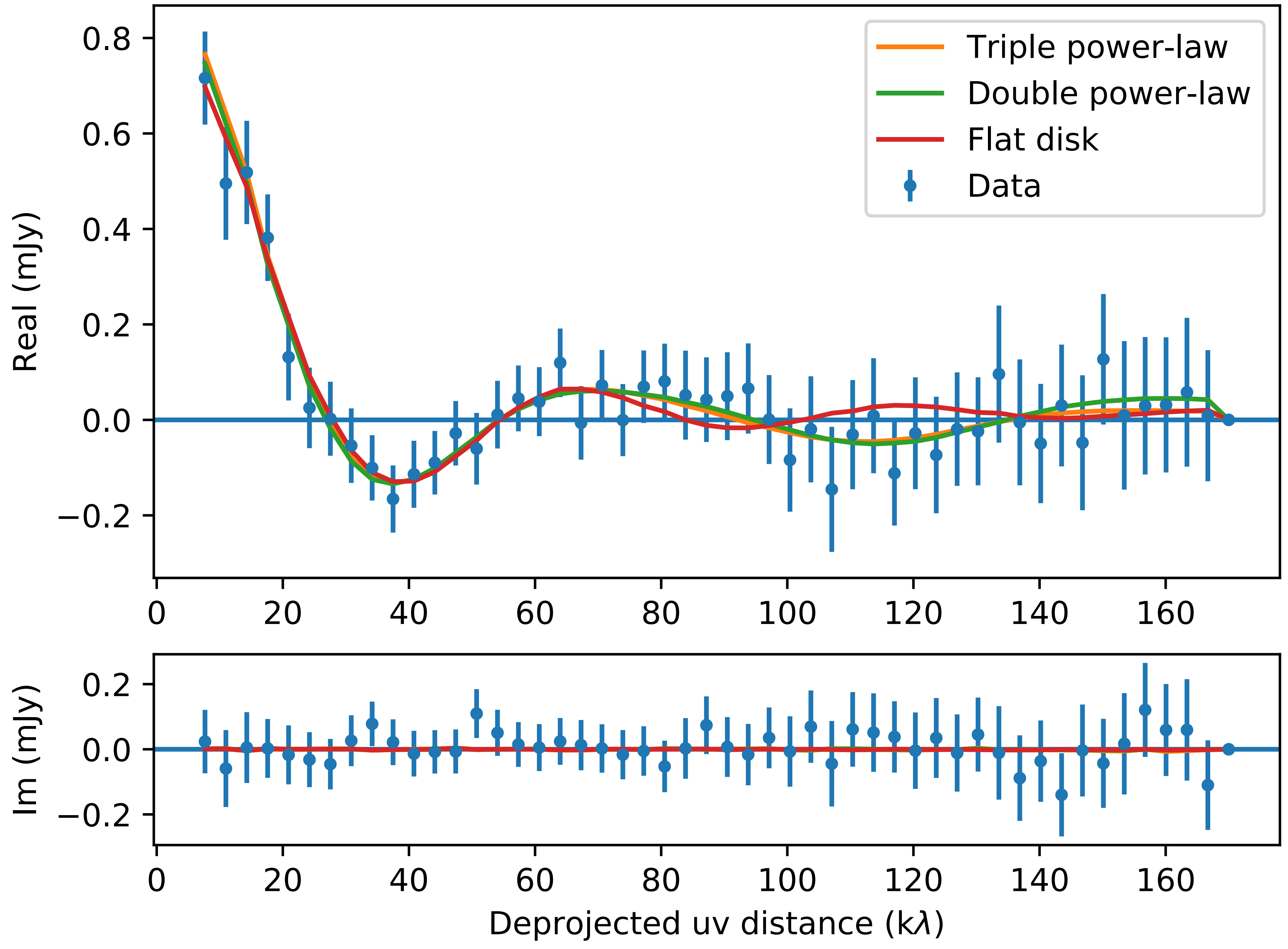

Figure 3. Elliptically averaged visibility profile comparing the data (blue points) with the best-fit flat disk (red line), double power-law with a gap (green line) and triple power-law (orange line) models. The top panel shows the real part of the visibilities while the bottom panel shows the imaginary part of the visibilities. The visibilities have been deprojected assuming an inclin... of 44° and a position angle of 60°, the best-fit values for the double power-law model.

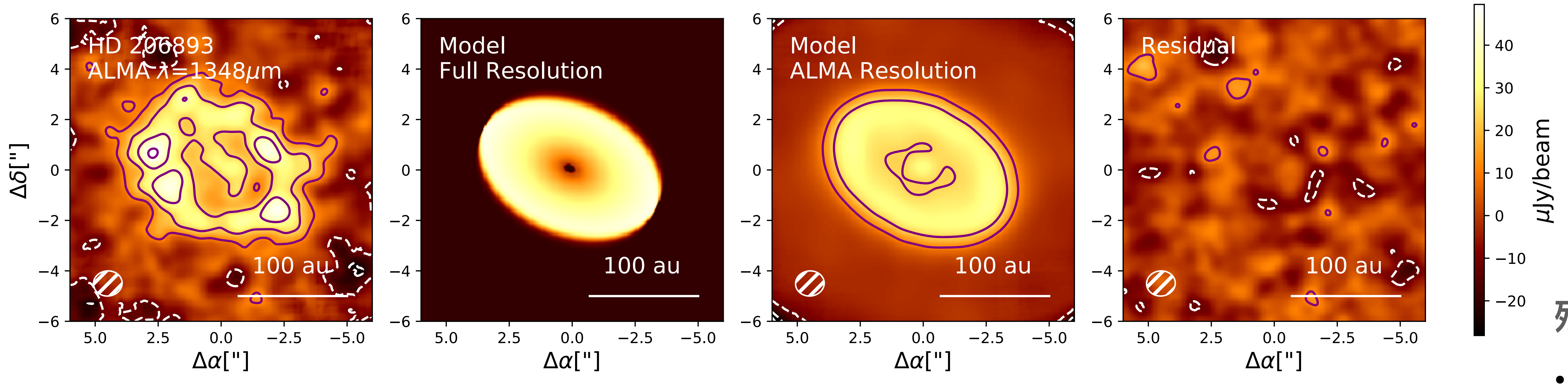

Figure 4. (Left) Naturally weighted ALMA image of the 1.3 mm continuum emission from the HD 206893 system, with a taper of 200 kλ applied to bring out the large-scale structure of the source. (Center Left) Full resolution model image for a flat disk showing the structure of the disk with a stellar flux equal to zero. (Center Right) Model image sampled at the same baseline lengths and orientations as the ALMA data, showing the best-fit model without a gap in the middle of the dust disk. (Right) Residual image after subtracting the model from the data in the visibility domain. Contour levels and symbols are as in Figure 1.

Table 3. MCMC Fitting Results

Parameter	Flat Disk		Double Power Law with Gap		Triple Power Law	
	Best Fit	Median	Best Fit	Median	Best Fit	Median
R_{in} (au)	9	$< 44^{a}$	21^{a}	$< 51^{a}$	35	29^{+7}_{-20}
ΔR(au)	155	151^{+14}_{-11}	176	166^{+20}_{-16}	159	164^{+18}_{-14}
Log($M_{\rm disk}$) ($M_\oplus$)	-1.66	$-1.63^{+0.03}_{-0.03}$	-1.61	$-1.63^{+0.03}_{-0.02}$	-1.74	$-1.74^{+0.07}_{-0.07}$
F_* (μJy)	16	19^{+6}_{-6}	17	18^{+5}_{-5}	14	15^{+5}_{-6}
PA (°)	66	63^{+3}_{-3}	60	59^{+3}_{-3}	60	63^{+3}_{-3}
i (°)	47	47^{+2}_{-2}	45	44^{+3}_{-3}	43	47^{+3}_{-3}
Δx (″)	0.11	$0.14^{+0.07}_{-0.07}$	0.16	$0.11^{+0.07}_{-0.09}$	0.11	$0.09^{+0.08}_{-0.09}$
Δy (″)	0.05	$0.04^{+0.06}_{-0.06}$	0.04	$0.03^{+0.05}_{-0.05}$	0.05	$0.06^{+0.11}_{-0.07}$
$R_{\rm in,Gap}$ (au)			67	63^{+8}_{-16}		
$\Delta R_{\rm Gap}$ (au)			32	31^{+11}_{-7}		
pp1			-2.0	$-1.1^{+1.1}_{-0.8}$	-2.7	$-1.2^{+0.8}_{-1.1}$
pp2			2.8	$3.0^{+1.0}_{-0.9}$	4.7	> 0.23
pp3					-3.7	$-3.0^{+1.3}_{-1.0}$
Rt1			97	102^{+16}_{-17}	73	71^{+9}_{-33}
Rt2					113	115^{+8}_{-7}
Ln prob	-10733015.1		-10732991.8		-10732995.1	

NOTE—[a] The inner radius is unresolved in the models without a gap, so the best-fit value of 9 au or 21 au is not meaningful. The upper limit of 44 au or 51 au represents the 99.7th percentile of the posterior distribution.

5. DISCUSSION

5.1. *Disk Structure Constraints*

残骸円盤の全体像

- 内径 < 51 AU；外径 ~194 AU (表の$R_{\rm in}+\Delta R$)⇨ 褐色矮星まわりの残骸円盤として最大(と言ってもサンプル数小)
- 方位角方向平均操作は妥当だった.
- mmサイズのダストが中心 $\lesssim$ 37 AUに存在しないと輝度分布を説明できない.

Planetesimal belt (邦訳は微惑星帯？)

- 残骸円盤円盤面とのなす角が大きい可能性を排除できない.

5.2. *Gap Detection and Implications*

ギャップ

- 図2-4の解析から, R~63 AUに幅30+/-10AUのギャップが 存在することは確実
  (⇦ 古屋疑問 ー Gapの幅、こんなに大きいのはBDまわりの残骸円盤だから？)
- ギャップの「今の姿」を説明するためには, 惑星による形成が自然で, ガスの運動, 化学進化によるみかけ上のギャップ形成説や磁気流体不安定性による形成説を積極的に支持する証拠はない.

5.3. *N-body Simulations of the Star, Brown Dwarf, and Putative Planet*

Table 5. Gap Width and Depth with Varying Brown Dwarf Parameters

BD Mass (M_{Jup})	BD Eccentricity	BD Inclination($^\circ$)	Gap Width (au)	Gap Depth (%)

Table 6. Gap Width and Depth with Varying Planet Parameters

Planet Mass ($M_\oplus$)	Planet Eccentricity	Planet Inclination ($^\circ$)	Gap Width (AU)	Gap Depth (%)

表5, 6にまとめた解析から

- 褐色矮星質量 = 15 Mjup,,,,,,

議論の焦点(のひとつ)/明らかにしたいこと：Gapped structureの起源

- (この残骸円盤中の巨大な)ギャップは, 原始惑星系円盤期から成長してきたものか? あるいは　the system(≃残骸円盤期と意訳してよい?)になってから形成されたものか?
- ⇨ 本研究だけからは定かでない.

論文タイトルをみたとき&読み始めの段階で, 私が知りたかったこと

- 褐色矮星を含む残骸円盤の初めてのALMA撮像観測なので, 惑星だけを含む残骸円盤(統計が無理であれば代表的なもの)との比較コメントを読みたかった(それほど意味のないことなのか?), 惑星に比べ, 輻射場は強いのであろうから, ダストの性質(1mm帯のみの観測だからβの議論は無理だが, NIRと合わせて何か議論できる?)に与える影響, ガス・ダスト比(COが検出できなかった上限値は強い制限にならなかったのか?)の議論など. ⇨ 今後の研究に期待

26. **Fiery Cores: Bursty and Smooth Star Formation Distributions across Galaxy Centers in Cosmological Zoom-in Simulations**
Matthew E. Orr, H Perry Hatchfield, Cara Battersby, Christopher C. Hayward, Philip F. Hopkins, Andrew Wetzel, Samantha M. Benincasa, Sarah R. Loebman, Mattia C. Sormani, Ralf S. Klessen ★ We present an analysis of the $R \lesssim 1.5$ kpc core regions of seven simulated Milky Way mass galaxies, from the FIRE-2 (Feedback in Realistic

(a)いくつかの銀河では, 非対称的なガス分布(必然的に非対称性のある星形成率分布) ⇨ CMZ全域にわたって離心率の大きい楕円軌道となり, ~10 Myrはつづく爆発的星形成

(b)それ以外び銀河では, 滑らかなガス分布(同, 星形成率分布)

ABSTRACT

We present an analysis of the $R \lesssim 1.5$ kpc core regions of seven simulated Milky Way mass galaxies, from the FIRE-2 (Feedback in Realistic Environments) cosmological zoom-in simulation suite, for a finely sampled period ($\Delta t = 2.2$ Myr) of 22 Myr at $z \approx 0$, and compare them with star formation rate (SFR) and gas surface density observations of the Milky Way's Central Molecular Zone (CMZ). Despite not being tuned to reproduce the detailed structure of the CMZ, we find that four of these galaxies are consistent with CMZ observations at some point during this 22 Myr period. The galaxies presented here are not homogeneous in their central structures, roughly dividing into two morphological classes; (a) several of the galaxies have very asymmetric gas and SFR distributions, with intense (compact) starbursts occurring over a period of roughly 10 Myr, and structures on highly eccentric orbits through the CMZ, whereas (b) others have smoother gas and SFR distributions, with only slowly varying SFRs over the period analyzed. In class (a) centers, the orbital motion of gas and star-forming complexes across small apertures ($R \lesssim 150$pc, analogously $|l| < 1°$ in the CMZ observations) contributes as much to tracers of star formation/dense gas appearing in those apertures, as the internal evolution of those structures does. These asymmetric/bursty galactic centers can simultaneously match CMZ gas *and* SFR observations, demonstrating that time-varying star formation can explain the CMZ's low star formation efficiency.

結論 そうは言うけど Cosmological なものかの コメントない

Keywords: Galaxy: center, star formation, ISM, spiral, ISM: kinematics and dynamics

今回, 解析したシュミレーション：先行研究から

Mon. Not. R. Astron. Soc. **000**, 000–000 (0000) Printed 13 November 2018 (MN LaTeX style file v2.2)

FIRE-2 Simulations: Physics versus Numerics in Galaxy

Philip F. Hopkins⋆[1], Andrew Wetzel[1,2,3]†, Dušan Kereš[4], Claude-A
Giguère[5], Eliot Quataert[6], Michael Boylan-Kolchin[7], Norman Murray
C. Hayward[9], Shea Garrison-Kimmel[1], Cameron Hummels[1], Robert
Paul Torrey[11], Xiangcheng Ma[1], Daniel Anglés-Alcázar[5], Kung-Yi Su[1],
Denise Schmitz[1], Ivanna Escala[1], Robyn Sanderson[1], Michael Y. Gr
Hafen[5], Ji-Hoon Kim[12], Alex Fitts[7], James S. Bullock[13], Coral Wheeler
Oliver D. Elbert[13], Desika Narayanan[14]

[1]*TAPIR, Mailcode 350-17, California Institute of Technology, Pasadena, CA 91125, USA*

2018

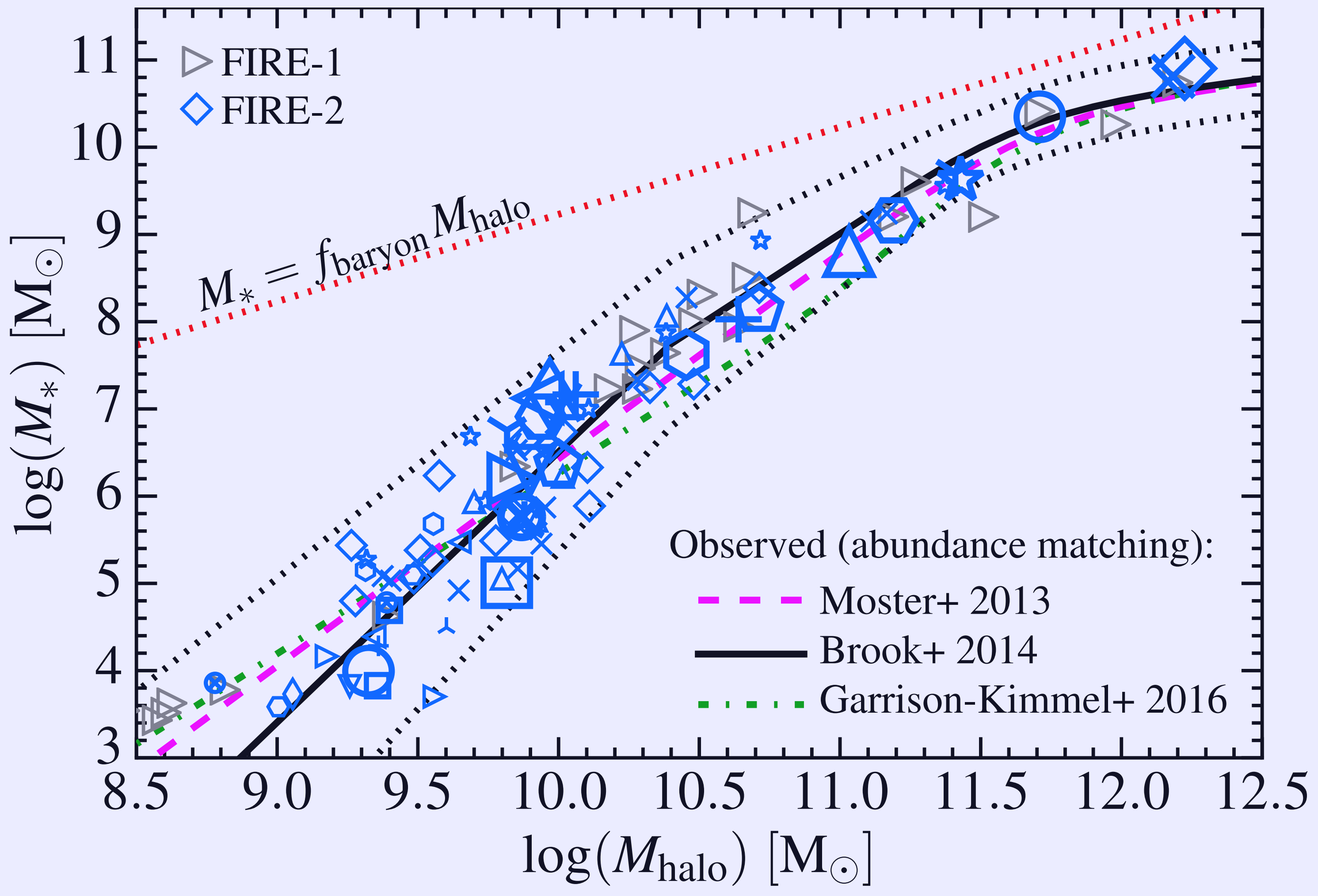

Figure 7. Stellar mass-halo mass relation for FIRE-2 simulations (colored points) at $z = 0$. Stellar masses and halo virial masses are defined as in Table 1, for all resolved, uncontaminated halos (116 galaxies total; see text, § 3). Large points show the "primary" (most massive) galaxy within the zoom-in region, in each simulation (different point styles). Grey triangles show FIRE-1 simulations. While individual galaxies may differ in mass, the effects are primarily stochastic: the two agree well on average. We compare observational estimates as labeled; black dotted lines show the observationally estimated $\sim 95\%$ intrinsic scatter (see text). Within the scatter and systematic variations between fits, the simulations agree well with the observations at all masses.

Table 2. Physics & Numerics Explored in This Paper (and Papers II & III)

Physics/Numerics	§	Effects in FIRE-2 Simulations	Guidelines / Default Choice
Resolution:			
Mass Resolution	4.1	Most results robust after resolving the Toomre scale, some (e.g. massive galaxy morphology) depend on resolved winds/hot gas	Resolution criteria in § 4.1.3 (Eq. 5-7)
Collisionless (DM/Stellar) Force Softening	4.2	Irrelevant unless extremely small or very large values used, adaptive collisionless softenings require additional timestep limiters	Optimal range of values in § 4.2.2
Gas Force Softening	4.2	Forcing fixed softening generally has no effect, unless too large, then fragmentation & SF are artificially suppressed	Fully-adaptive softenings (matching gas) should be used
Timestep Criteria	4.3	Provided that standard stability criteria are met, this has no effect. Additional limiters needed for stellar evolution & adaptive softening	Standard limiters + Stellar (Eq. 12) + Adaptive softening (Eq. 13)
(Magneto)-Hydrodynamics:			
Hydro Method (MFM vs. SPH)	5	Irrelevant for dwarfs. Important for massive galaxies with hot halos. SPH may suppress cooling & artificially allows clumpy winds to vent	Newer methods recommended
Artificial Pressure "Floors"	6	Unimportant unless set too large, then prevents real fragmentation. Double-counts "sub-grid" treatment of fragmentation with SF model	Do not use with self-gravity based SF models
Magnetic Fields, Conduction, Viscosity	F	Weak effects on sub-galactic scales (dense gas, morphology, turbulent ISM) (Not studied here, but in Su et al. 2017; effects in CGM could be larger)	See Su et al. (2017)
Metal Diffusion (sub-resolution mixing)	7.2 & F	Small effects on galaxy properties & dynamics, but potentially important for abundance distributions of stars	Best practice depends on numerical hydro method
Cooling:			
Molecular Chemistry/Cooling	7 & B	No effect on galaxy properties or star formation (just a tracer). Not important star formation criterion if fragmentation is resolved	May be relevant at $[Z/H] \ll -3$, can be important for observational tracers
Low-Temperature Cooling ($T \ll 10^4$ K)	7 & B	Details have no dynamical effects because $t_{\rm cool} \ll t_{\rm dyn}$ in cold gas to opacity limit ($\sim 0.01\,M_\odot$). Relevant for observables in cold phase	*Some* needed to form cold clouds, details dynamically irrelevant
Metal-Line Cooling ($T \gtrsim 10^4$ K)	7 & B	Dominates cooling in metal-rich centers of "hot halos" around massive galaxies, and of individual SNe blastwaves	Needed: important in super-bubbles & "hot halos"
Photo-Heating (Background)	7 & B	Significantly suppresses star formation in small ($M_{\rm halo} \lesssim 10^{10}\,M_\odot$) dwarfs	Needed: dwarfs & CGM/IGM
Star Formation:			
Self-Gravity (Virial) Criterion	8 & C	Negligible effect on galaxy properties (SF is feedback-regulated). More accurately identifies collapsing regions in high-dynamic range situations	Recommended; see Appendix C for implementation
Density Threshold	8 & C	Negligible effect on galaxy properties (SF is feedback-regulated) Can be arbitrarily high with adaptive gas softenings	Should exceed galactic mean density; ideally, highest resolved densities
Jeans-Instability Criterion	8 & C	Negligible effect on galaxy properties (SF is feedback-regulated). Automatically satisfied in high-density, self-gravitating gas	Not necessary
Self-shielding/Molecular Criterion	8 & C	Negligible effect on galaxy properties (SF is feedback-regulated). Automatically satisfied in high-density, self-gravitating gas	Not necessary
"Efficiency" (Rate) at Resolution Limit	8 & C	Negligible effect on galaxy properties (SF is feedback-regulated). If artificially lowered, more dense gas "piles up" until same SFR achieved	$\sim 100\%$ per free-fall in *locally-self-gravitating* gas
Stellar Feedback:			
Continuous Mass-Loss (OB & AGB)	9 & A	Primarily important as a late-time fuel source for SF Relatively weak "primary" feedback effects on galactic scales	Couple as Appendix D. Rates given in § A
Supernovae (Ia & II) ("How to Couple")	A & D Paper II	Type-II: Dominant FB mechanism on cosmological scales. Need to account for *PdV* work if Sedov phase un-resolved. Subgrid models should reproduce exact solutions, conserve mass, energy, & momentum, and converge	Couple as Appendix D. Validation & convergence tests & criteria in Paper II
Radiative Feedback (Photo-Heating & Radiation Pressure)	A & E Paper III	"Smooths" SF in dwarfs (less bursty) & suppresses SF in dense gas. UV background dominates in dwarfs. Photo-electric heating unimportant. IR multiple-scattering effects weak, except in massive galaxy nuclei.	Need photo-heating & single-scattering rad. pressure (Paper I Rad.-hydro algorithm sub-domin

今回, 解析したシュミレーション：先行研究から

The Astrophysical Journal Letters, 827:L23 (6pp), 2016 August 20
doi:10.3847/2041-8205/827/2/L23

RECONCILING DWARF GALAXIES WITH ΛCDM COSMOLOGY: SIMULATING A REALISTIC POPULATION OF SATELLITES AROUND A MILKY WAY–MASS GALAXY

Andrew R. Wetzel[1,2,3,8,9], Philip F. Hopkins[1], Ji-hoon Kim[1,4,10], Claude-André Faucher-Giguère[5], Dušan Kereš[6], and Eliot Quataert[7]

Low-mass "dwarf" galaxies represent the most significant challenges to the cold dark matter (CDM) model of cosmological structure formation. Because these faint galaxies are (best) observed within the Local Group (LG) of the Milky Way (MW) and Andromeda (M31), understanding their formation in such an environment is critical. We present first results from the Latte Project: the Milky Way on Feedback in Realistic Environments (FIRE). This simulation models the formation of an MW-mass galaxy to $z = 0$ within ΛCDM cosmology, including dark matter, gas, and stars at unprecedented resolution: baryon particle mass of 7070 $M_\odot$ with gas kernel/softening that adapts down to 1 pc (with a median of 25–60 pc at $z = 0$). Latte was simulated using the GIZMO code with a mesh-free method for accurate hydrodynamics and the FIRE-2 model for star formation and explicit feedback within a multi-phase interstellar medium. For the first time, Latte self-consistently resolves the spatial scales corresponding to half-light radii of dwarf galaxies that form around an MW-mass host down to $M_{star} \gtrsim 10^5\, M_\odot$. Latte's population of dwarf galaxies agrees with the LG across a broad range of properties: (1) distributions of stellar masses and stellar velocity dispersions (dynamical masses), including their joint relation; (2) the mass–metallicity relation; and (3) diverse range of star formation histories, including their mass dependence. Thus, Latte produces a realistic population of dwarf galaxies at $M_{star} \gtrsim 10^5\, M_\odot$ that does *not* suffer from the "missing satellites" or "too big to fail" problems of small-scale structure formation. We conclude that baryonic physics can reconcile observed dwarf galaxies with standard ΛCDM cosmology.

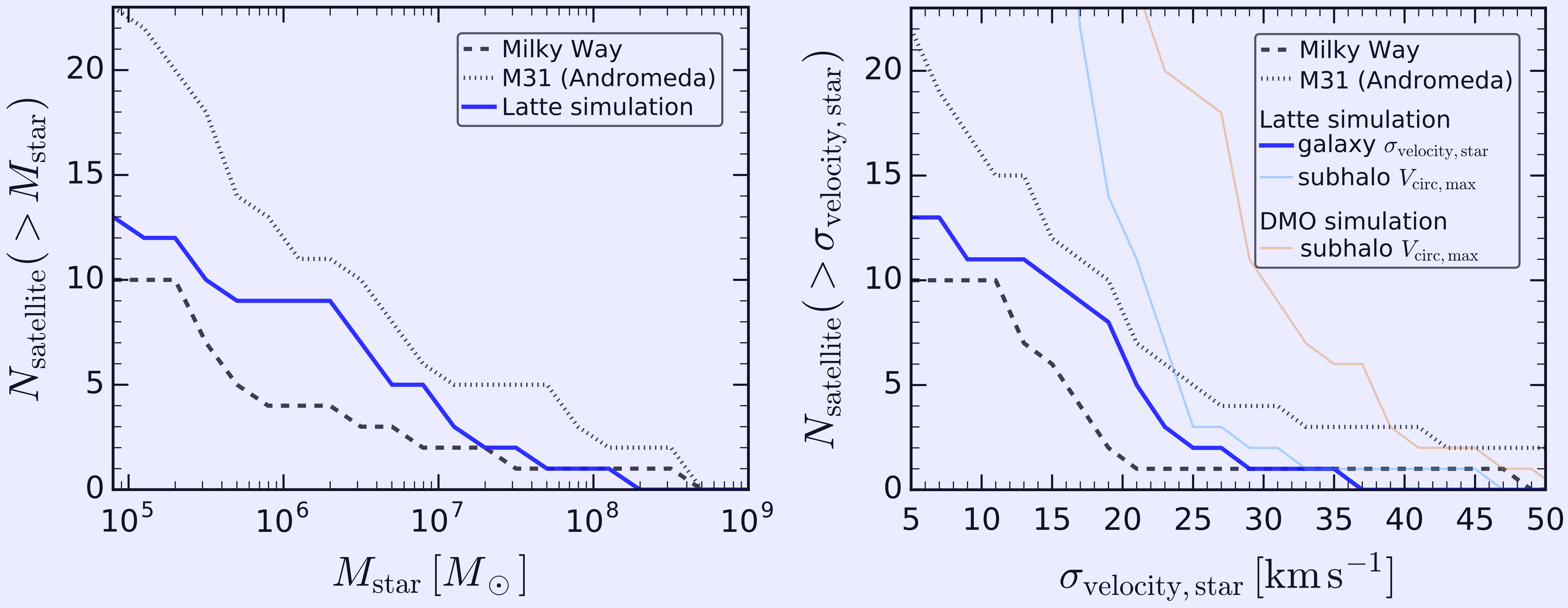

Figure 3. Cumulative number of satellites at $z = 0$ above a given stellar mass (left) and stellar 3D velocity dispersion (right) in the Latte simulation (blue) and observed around the Milky Way (MW; dashed) and Andromeda (M31; dotted), excluding the LMC, M33, and Sagittarius. For both M_{star} and σ, Latte's satellites lie entirely between the MW and M31, so Latte does not suffer from the "missing satellites" or "too big to fail" problems. Thin curves (right) show $V_{circ,max}$ for *all* dark-matter subhalos in the baryonic (light blue) and dark-matter-only (DMO; orange) simulations, demonstrating the ≈3× reduction from baryonic physics.

2. METHODS

We analyze the central regions the seven Milky Way/Andromeda-mass spiral galaxies from the 'standard physics' Latte suite of FIRE-2 simulations introduced in Wetzel et al. (2016) and Hopkins et al. (2018). The spatially resolved properties of the gas surface densities, velocity dispersions, and SFRs across the disks of these galaxies have been studied in detail in Orr et al. (2020). This work makes use of 11 snapshots finely spaced in time ($\Delta t \approx 2.2$ Myr) at $z \approx 0$ for each of the simulations. A brief summary of the $z \approx 0$ global properties of the galaxy simulations are included in Table 1 of Orr et al. (2020).

時間分解能

The simulations analyzed here all have minimum baryonic particle masses of $m_{b,min} = 7100$ M$_\odot$, minimum adaptive force softening lengths <1 pc, and a 10 K gas temperature floor. With adaptive softening lengths, we note that the median softening length within the disk in the runs at $z = 0$ is $h \sim 20 - 40$ pc (at a $n \sim 1$ cm^{-3}), with the dense turbulent disk structures having necessarily shorter softening lengths. The aperture sizes considered in this work are $145 - 500$ pc[1], and so are well above the minimum resolvable scales in the simulations.

空間分解能

Importantly, for discussion here: star formation in the simulations occurs on a free-fall time in gas which is dense ($n > 10^3$ cm^{-3}), molecular (per the Krumholz & Gnedin 2011 prescription), self-gravitating (viral parameter $\alpha_{\rm vir} < 1$) and Jeans-unstable below the resolution scale. Once these requirements are met, the SFR at the particle scale is assumed to be: $\dot{\rho}_\star = \rho_{\rm H_2}/t_{\rm ff}$ (*i.e.*, 100% efficiency per free-fall time). Star particles are treated as single stellar populations, with known age, metallicity, and mass. Feedback from supernovae, stellar mass loss (OB/AGB-star winds), photoionization and photoelectric heating, and radiation pressure are explicitly modeled. These simulations do not include any supermassive black holes (SMBHs), and accordingly do not have any feedback associated with BH accretion, nor do they include cosmic rays or other MHD physics. Detailed descriptions of these physics and their implementation can be found in Hopkins et al. (2018).

ガス塊を星に置き換える条件

考慮した現象

考慮していない現象

結果

(a)いくつかの銀河では, 非対称的なガス分布(必然的に非対称性のある星形成率分布) ⇨ CMZ全域にわたって離心率の大きい楕円軌道となり, ~10 Myrはつづく爆発的星形成

erties of our Galactic center. Within the sample of seven galaxies, we see two distinct classes of central morphology in their *fiery cores* (gas and star formation distributions within $R \approx 1.5$ kpc):

(a) "Asymmetric/Bursty" (**m12b**, **m12c**, **m12f**, & **m12w**): Large, asymmetric gas clouds and star-forming complexes are seen. Star formation is concentrated in intense starbursts whose feedback dramatically shapes the local gas environment (see **m12b**, upper subfigure of Fig. 1). Two simulations falling in this category (**m12b** & **m12f**) simultaneously match the MW CMZ gas *and* SFR measurements. The two others (**m12c** & **m12w**) do not simultaneously have SFR *and* dense gas tracers within the central 145 pc *at any point in this time window.*

(b) "Smooth" (**m12i**, **m12m**, & **m12r**): Gas and star formation is smoothly distributed within the galactic centers, with clear feeding of gas into center, and a cirrus of star formation (see **m12m**, lower subfigure of Fig. 1). Feedback events do not dramatically alter the local gas environment, as the feedback is relatively dispersed across their centers.

Interestingly, none of the galaxies here exhibit the ring structures, presumed to be long-lived, seen by studies of the central regions of other spiral galaxies and the

どちらのタイプの渦巻銀河でも長寿命のリング構造は確認されず

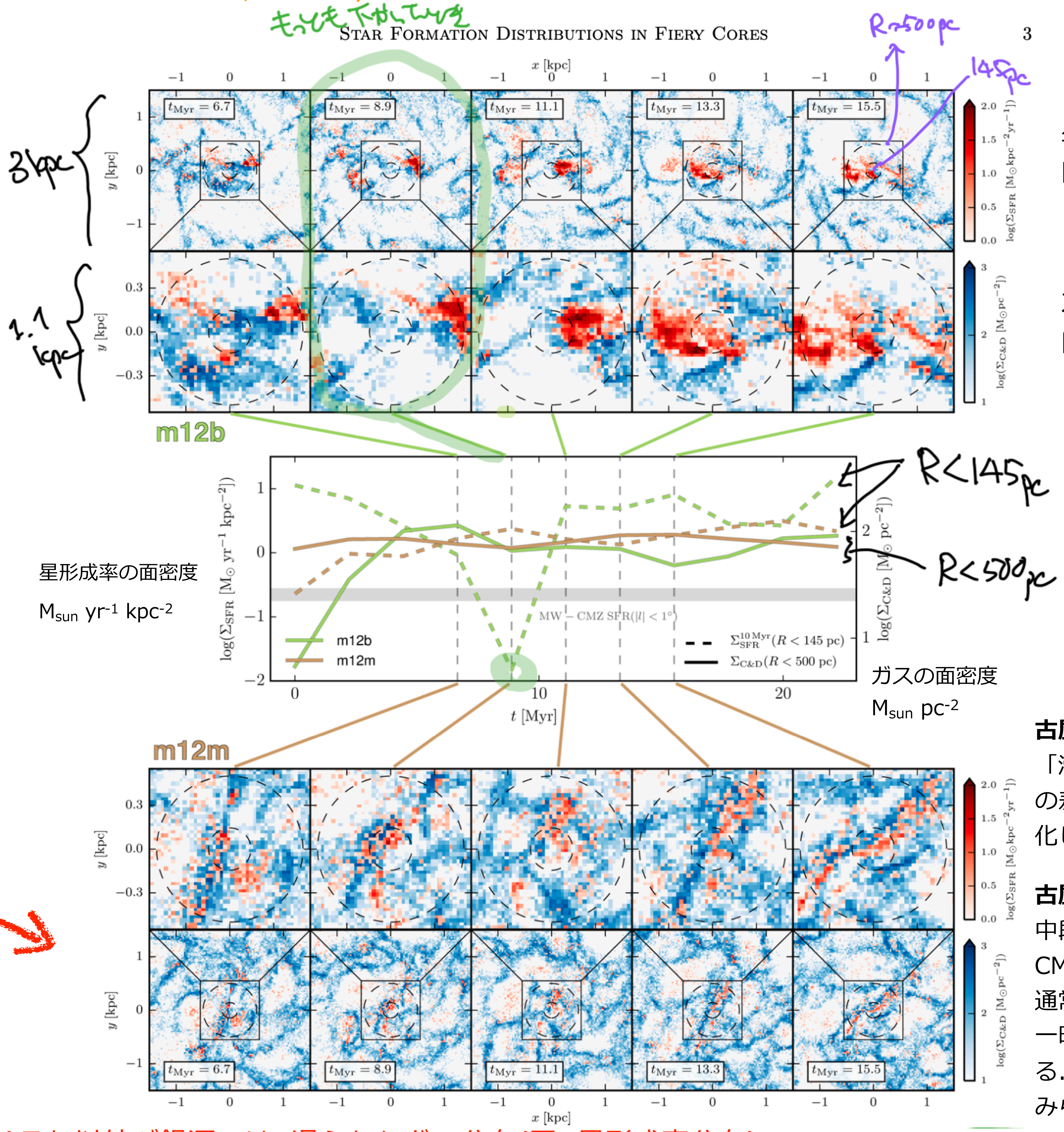

(b)それ以外び銀河では, 滑らかなガス分布(同, 星形成率分布)

星形成率の面密度
Msun yr^{-1} kpc^{-2}

ガスの面密度
Msun pc^{-2}

天の川のCMZと比べるとき, *R*<145 pc を見てください。
(|*l*| ≲ 1° at *d* of ~8.2 kpc)

緑は上のタイプの銀河,
茶色は下のタイプの銀河

古屋納得しきれていない点

「滑らか」と言われても緑と茶色の銀河での差は, 目でみた範囲ではわからない(定量化してほしい).

古屋理解しきれていない点

中段パネルの点線は明らかに灰色帯(天の川CMZ)より上にある. これが渦巻銀河中心部の通常の姿という主張か？
一時的に低減することは, 緑の破線からわかる. しかし, 本文でいうstarburstはここではみられない.

天の川のCMZと比べるとき,
R<145 pc を見てください。
($|l| \lesssim 1^{\circ}$ at d of ~8.2 kpc)

結果

SFR みつど

面みつど

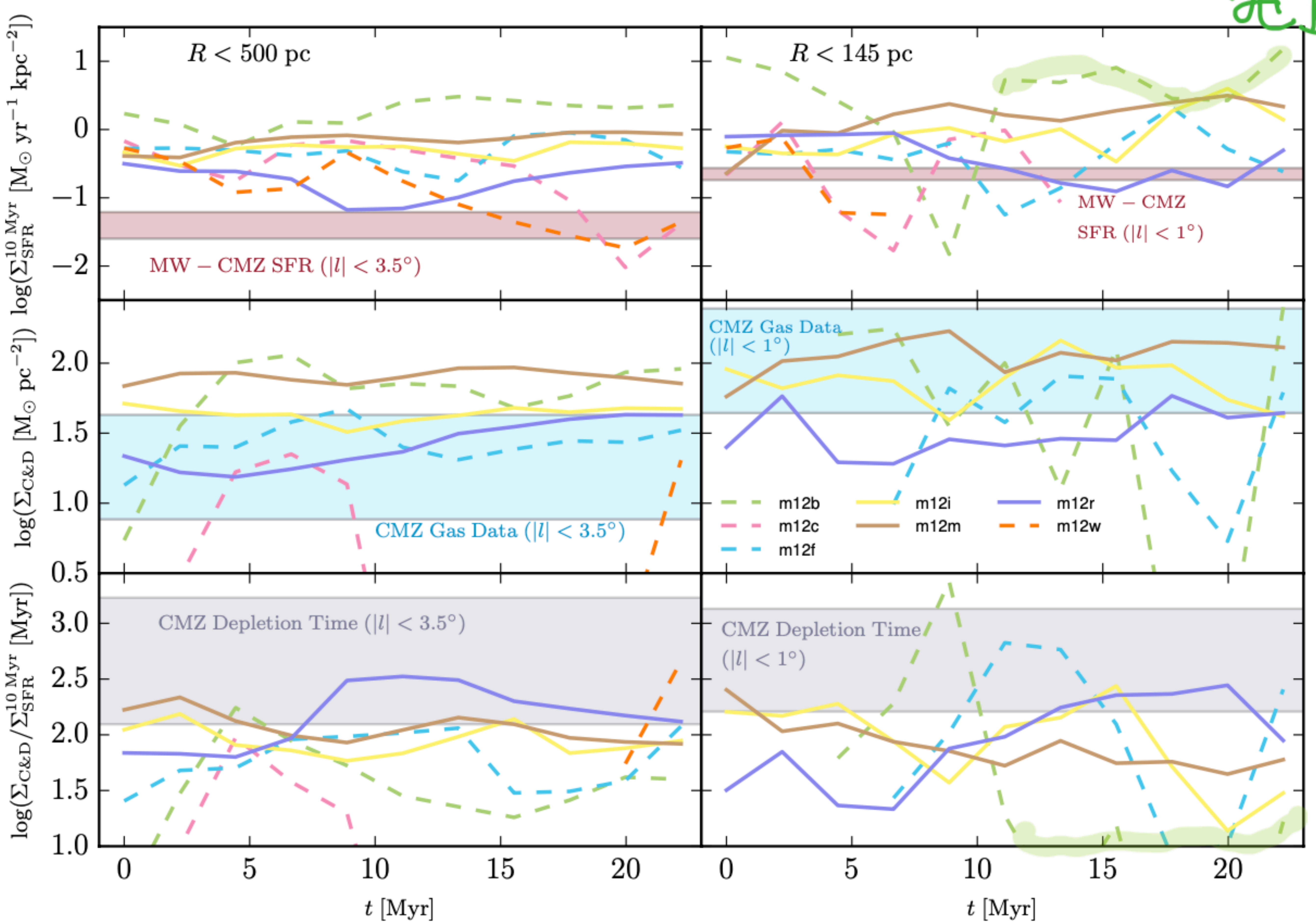

なぜ上がったまま? なのか?

ガスの枯渇時間 = ガスの平均面密度を星形成率面密度を10 Myrsにわたって積分したもので除した.

Myrs

灰色帯は天の川CMZ

Figure 2. SFRs and cold & dense (C&D) gas surface densities in central regions of seven FIRE-2 spiral galaxies (colored lines; "class (a)/(b)" plotted with dashed/solid lines, respectively), for $R < 500$ (left column) and $R < 145$ pc (right column) apertures, as a function of time near $z \approx 0$ ($\Delta t \approx 2.2$ Myr, rightmost edge being $z = 0$). Shaded bands indicate SFR and gas surface density observations, with uncertainty, of the CMZ from Longmore et al. (2013) and Mills & Battersby (2017), respectively. Depletion times ($\Sigma_{C\&D}/\Sigma_{SFR}^{10\,Myr}$) are also presented, in the same style; these CMZ depletion times are produced by combining Longmore et al. (2013) and Mills & Battersby (2017) data. SFRs evolve more smoothly in all galaxies in larger apertures ($R < 500$ pc), and the variance in SFRs or gas surface density increases with smaller apertures. However, in the simulations, two central molecular zone classes appear to exist on $R < 145$ pc scales: galaxies like **m12b** and **m12c** with very asymmetric gas distributions and dramatic starbursts on ~ 10 Myr timescales, "class (a)"; and galaxies like **m12i** and **m12m** typifying smoother (though still with non-trivial fluctuations) SFR and gas distributions in their centers, "class (b)" (see, **m12b** and **m12m** in Fig. 1 as examples of classes (a) and (b), respectively). Despite temporal and spatial variance, many of the FIRE galaxies are consistent with MW CMZ observations *at some point* in this time-window.

古屋理解しきれていない点

緑の破線の振る舞い(手書きメモ箇所). ガスが枯渇したあともSFR密度があがったままの銀河あるのは, なぜ？

結果

Fig 1 中野に示すと 合っていないような？

RR ET AL.

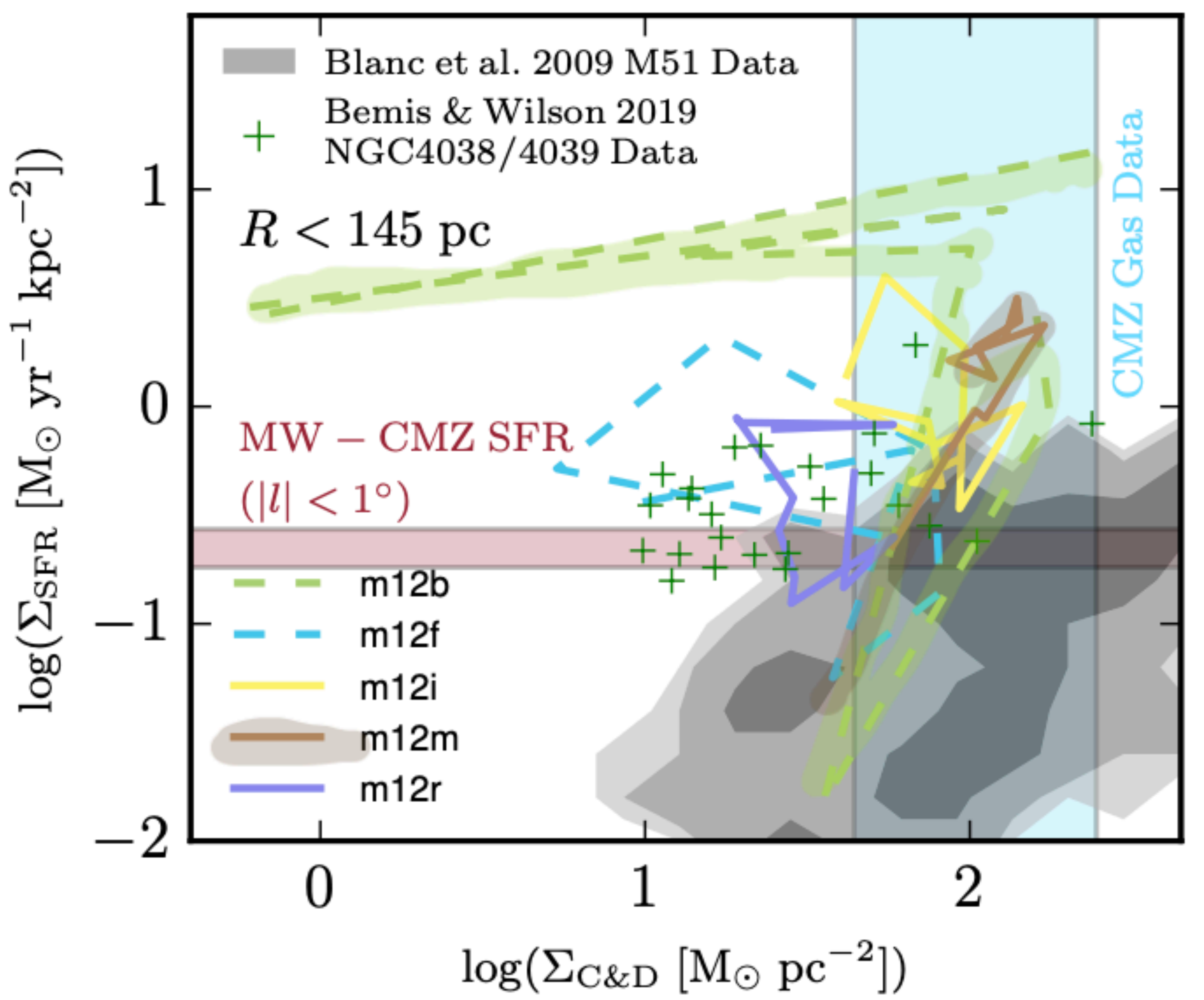

Figure 3. KS relation in central regions of the five FIRE-2 spiral galaxies (colored lines: "asymmetric" centers plotted with dashed lines, "smooth" centers with solid lines) that ~~simultaneously~~ have SFR and dense gas tracers within the $R < 145$ pc aperture, as a function of time near $z \approx 0$ ($\Delta t \approx 2.2$ Myr). CMZ SFR and gas estimates, with uncertainty, (Longmore et al. 2013 and Mills & Battersby 2017) plotted as horizontal and vertical shaded bands, respectively, and spatially resolved KS observations (~ 170 pc & ~ 675, respectively) of M51 (Blanc et al. 2009, their X_{CO} adjusted to be consistent with MW value) and the Antennae Galaxies (NGC 4038/9; Bemis & Wilson 2019) plotted in greyscale contours and with green '+'s, respectively. The central regions of some galaxies remain fairly stable in KS-space over 22 Myr (*e.g.*, **m12m**), whereas others (*e.g.*, **m12b**) vary by upwards of a dex in both SFR and $\Sigma_{C\&D}$. Four FIRE galaxies (**m12b**, **m12f**, **m12m**, & **m12r**) overlap with the CMZ SFR estimate at various times.

最後にKS則と合っていることを示したいらしい

水色とピンクの帯は, 天の川銀河CMZ

少なくとも解析した7つの銀河の値は, 帯の交差部分付近にくる(⇦それってすでにFigs.1&2で示したことじゃないの？. さらにその時間変化の軌跡は, KS則と大きな矛盾はない.

議論に付言されていたこと

バーエンドでの星形成率↑は, 定常的で大きく時間変化しない.

素人のツッコミ, 解釈

KS則と比較するためには, ガス面密度方向のダイナミックレンジが小さすぎる.

KS則との整合性の文脈でみるよりかは, むしろ, 帯の交差部分よりもシミュレーション点がひろがっていることや(緑の線に見られるように)KS則からずれた軌跡を描く中心領域が多いことは, KS則成立はあくまでも, いわゆる円盤部だけでは？ ⇨ むしろ星形成のモードの議論へのヒントになるのでは？

SMBHフィードバック、特にsuperwindなどを考慮しないでも, ある程度, 説明できるのですね.

銀河シュミレーションの結果という意味では, 私の知る限りでは, 特段新しい知見(物理の提案)はなかった. この論文がApJ Lettersに受理された大きな理由は, cosmologicalなシュミレーションから出発して, $z = 0$の銀河の中心領域の振る舞いをそれなりにそれなりの分解能で(Δt~2Myrs, 数100 pc = JCMTで数Mpcの銀河を観測する分解能)再現できたことではないか？

Principal component analysis tomography in near-infrared integral field spectroscopy of young stellar objects. I. Revisiting the high-mass protostar W33A

F. Navarete[1]★, A. Damineli[1], J. E. Steiner[1]†, R. D. Blum[2]
[1] *Universidade de São Paulo, Instituto de Astronomia, Geofísica e Ciências Atmosféricas, Rua do Matão 1226, Cidade Universitária São Paulo-SP, 05508-090, Brasil*
[2] *NSF's Optical–Infrared Astronomy Research Laboratory P.O. Box 26732, Tucson, AZ 85719, USA*

Accepted 2021 February 4. Received 2021 February 4; in original form 2020 November 29

COの吸収線から回転曲線

★ Mdisk : ~10M☉

ABSTRACT
W33A is a well-known example of a high-mass young stellar object showing evidence of a circumstellar disc. We revisited the *K*-band NIFS/Gemini North observations of the W33A protostar using principal components analysis tomography and additional post-processing routines. Our results indicate the presence of a compact rotating disc based on the kinematics of the CO absorption features. The position-velocity diagram shows that the disc exhibits a rotation curve with velocities that rapidly decrease for radii larger than 0.″1 (~250 AU) from the central source, suggesting a structure about four times more compact than previously reported. We derived a dynamical mass of $10.0^{+4.1}_{-2.2}$ $M_\odot$ for the "disc+protostar" system, about ~33% smaller than previously reported, but still compatible with high-mass protostar status. A relatively compact H_2 wind was identified at the base of the large-scale outflow of W33A, with a mean visual extinction of ~63 mag. By taking advantage of supplementary near-infrared maps, we identified at least two other point-like objects driving extended structures in the vicinity of W33A, suggesting that multiple active protostars are located within the cloud. The closest object (Source B) was also identified in the NIFS field of view as a faint point-like object at a projected distance of ~7,000 AU from W33A, powering extended *K*-band continuum emission detected in the same field. Another source (Source C) is driving a bipolar H_2 jet aligned perpendicular to the rotation axis of W33A.

Key words: methods: statistical – techniques: imaging spectroscopy – stars: protostars – stars: pre-main sequence – ISM: jets and outflows – ISM: individual: W33A

Gemini Northで2008年に取得した面分光データのトモグラフィ plus PCA再解析

導出された, 科学的な結果はそれほど画期的ではないかもしれないが, 手法がユニークで"変数分離"に成功 ⇨ PC *n*成分ごとに何らかの天体構造の抽出に成功 (n=5まで析している.)

We reconstructed the data cube using only the first five Principal Components which represents 99.996% of the variance and from this data cube we derive the following conclusions:

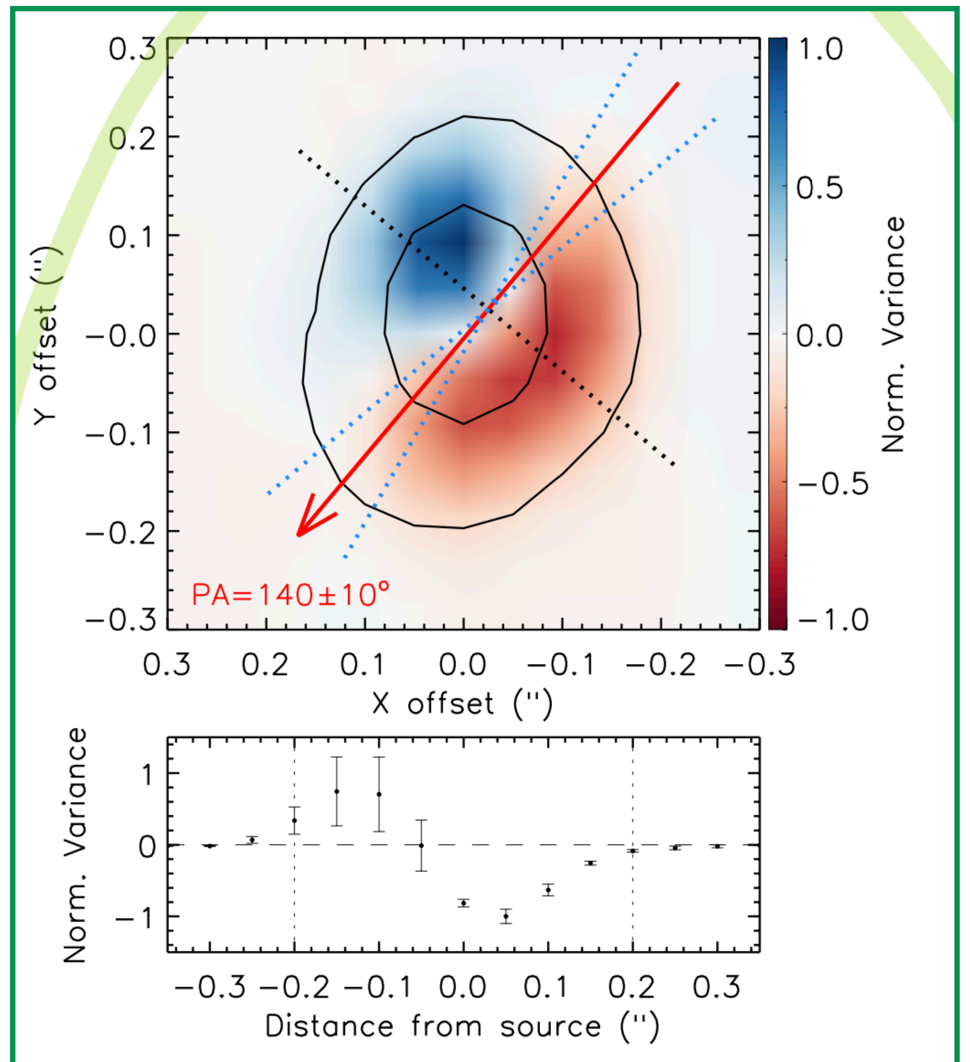

Figure 13. A detailed view of the disc-like structure probed by the PC3 tomogram. Top panel: The normalised variance of the tomogram is shown in a divergent red-to-blue colour-scale. The position of the compact source is indicated by the black contours. The red arrow and blue dashed lines indicate the position angle of the rotation axis of the disc and its error, respectively, estimated as PA = 140 ± 10°. The dashed black line shows the direction from which the radial variance profile was extracted. Bottom: the radial variance profile extracted along the plane of the disc. The points and error bars correspond to the mean variance and the 1-σ error of a 3-pixel width region perpendicular to the sampled spatial direction. The dashed vertical lines indicate the region where the absolute value of the variance is larger than zero ($|r| \leq 0.''2$).

5 CONCLUSIONS

We presented a reanalysis of the *K*-band NIFS/Gemini North observations of the protostar W33A, first done by D10, based on Principal Component Analysis Tomography. The PCS technique is well adapted to the analysis of complex data sets like the one analysed here.

(i) The PCA tomography was able to recover the spectral and spatial information of structures associated with the three key-ingredients of the disc-mediated accretion scenario of the high-mass star formation process: the cavity of the large-scale outflow probed by the ionised hydrogen, a rotating disc-like structure probed by the CO absorption features, and a wide-angle wind traced by the H_2 emission. All these structures were present in the first five Principal Components of the PCA Tomography. In addition, the technique also reveals structures with different kinematics (e.g. the rotation of the disc and the extended wind structure) in a much more efficient way than investigating each spectral feature using traditional methods.